



Projections on climate internal variability and climatological mean at fine scales over South Korea

Manh Van Doi¹ · Jongho Kim¹

Published online: 3 May 2020
© Springer-Verlag GmbH Germany, part of Springer Nature 2020

Abstract

Climate internal variability (CIV) plays an important role in understanding climate and is one of the principal uncertainties in climate projections. This study aims to estimate CIV and climatological mean (CM) in predictions using different emission scenarios for South Korea. A stochastic weather generator is employed to generate 100 ensembles of 30-year hourly time series for 40 meteorological stations. CIV is then estimated from the detrended method and compared with the noise computed by the two approaches. The extremely high value of the coefficient of determination between CIV values and noise indicates that the methodologies are seamless. The key results of this study include: (1) national average CM and CIV will increase in the future, and that increase will be greater in Representative Concentration Pathway 8.5 and end periods; (2) the nature of future changes in CM and CIV differ according to the indices of interest. Characteristics of three precipitation-quantity indices (total precipitation, totPr; daily maximum precipitation, maxDa; and hourly maximum precipitation, maxHr) and the precipitation-occurrence index (the number of days without precipitation, nonPr) are largely distinct; (3) examining the relationship between factors of changes of CIV and CM reveal a high correlation between them for maxDa and maxHr, but not for other indices; (4) The tail information of distribution for the FOC ratio implies that future changes in total and extreme precipitation are likely to be decoupled for some months or at some locations. The degree of decoupling is more noticeable on the hourly than the daily scale; and (5) the spatial deviation of CIV is also larger during the summer when CIV values are spatially large; this is valid only for totPr and maxDa. Methodologies and results for finer scales help assess the impact of climate change and develop appropriate adaptation and response strategies.

Keywords Climate internal variability · Climatological mean · Future projection · Finer scales · Weather generator · Spatial distribution · Factors of change

1 Introduction

Climate internal variability (CIV) in the form of such phenomena as El Niño–Southern Oscillation (ENSO) and thermohaline circulation is an essential part of understanding climate (Deser et al. 2012a, b, 2014; Frankcombe et al. 2015). The term refers to natural internal variability caused by complex feedbacks and nonlinear interactions

among intrinsic components of a climate system, and is a comparative concept of climate external variability affected by anthropogenic or natural changes in external forcing (Deser et al. 2012a, b; IPCC 2013; Thompson et al. 2015; Aalbers et al. 2017). Due to its physical significance, the notion of internal variability has long been studied in climatology and appears in the form of various terminologies in other disciplines, for example, “endogenous” in geology, “autogenic” in sedimentology, and “internal” in hydro-geomorphology (Kim et al. 2016a). In general, the short-term (within two weeks) predictability of climate variability is relatively reliable in daily weather forecasts (Simmons and Hollingsworth 2002; Domeisen et al. 2018; Scaife and Smith 2018). However, it is challenging to predict CIV on larger time horizons such as the next 50 or 100 years, even if uncertainties about climate models and external forcing have been resolved (Hawkins and Sutton

Electronic supplementary material The online version of this article (<https://doi.org/10.1007/s00477-020-01807-y>) contains supplementary material, which is available to authorized users.

✉ Jongho Kim
kjongho@ulsan.ac.kr

¹ School of Civil and Environmental Engineering, University of Ulsan, Ulsan, South Korea

2009; Deser et al. 2012a; Addor and Fischer 2015). Clearly defining and quantifying CIV in climate projections is therefore necessary for providing reliable forecasts and improving decision-making.

Prediction of CIV has been performed mainly by generating an ensemble from model simulation results and calculating the degree of spread among the ensemble members. Ensemble-generation can be classified by four approaches using dynamic, analytical, statistical, and stochastic models (Kim et al. 2018). The dynamic method employs a deterministic climate model to create a large number of simulations, with only minor modifications to the initial conditions of the atmospheric component. External forcings and the initial conditions of the other model components are constrained to be identical (Deser et al. 2012a, b, 2014; Fischer et al. 2013; Fischer and Knutti 2014; Hu et al. 2018). Sensitivity to the initial conditions is mostly deemed a component that causes the internal variability. The analytic approach can estimate the range of CIV from an analytic mathematical model, but several key assumptions for the probability distribution of internal variability, the trend of climate change, and the stationarity of two statistics used are essential (Thompson et al. 2015). The statistical and stochastic approaches are comparable in that they build an ensemble directly from historical observations. However, they can be further classified according to whether they allow for climatic stochasticity in future projections and whether historically unobserved realizations are fully explored. The statistical approach often underestimates the variability of a climate system compared to the stochastic approach which better reproduces the stochastic nature of natural climate variables (Hingray and Said 2014; Kim et al. 2018). Kim et al. (2018) explore the advantages and disadvantages of the four approaches in more detail.

The contribution of CIV to total uncertainty in a future projection can be substantial (Hawkins and Sutton 2009, 2010; Deser et al. 2012a, b, 2014; Fischer et al. 2014; Hingray and Said 2014; Kim and Ivanov 2015; Xie et al. 2015; Monerie et al. 2017; Martel et al. 2018). However, mixed results have been reported depending on spatial and temporal scales, locations, and climate indices. First, future CIV averaged over the globe decreases for mean precipitation (Hingray and Said 2014; Dai and Bloecker 2018) and mean temperature (Hawkins et al. 2015; Olonscheck and Notz 2017). In contrast, future CIV averaged over geographical regions (at regional scales) remains unchanged (Hawkins and Sutton 2010; Thompson et al. 2015), increases for mean precipitation (Pendergrass et al. 2017), or decreases for mean temperature (Hawkins et al. 2015). At local scales, future CIV for computational cells (2 or 12 km resolution) will be unchanged for mean precipitation (Peleg et al. 2019). Second, no consistent results were

found regarding the temporal scale. Internal variability for global mean precipitation on a decadal scale (Hawkins and Sutton 2010) and natural climate variability on a daily scale (Peleg et al. 2019) were unchanged. Internal variability decreases slightly for annual precipitation on an annual scale (Lafaysse et al. 2014), or increases over almost all land areas on a daily scale (Pendergrass et al. 2017). Third, CIV greatly varies depending on location. When looking at spatial distributions over different regions or locations, CIV is high in polar and tropical regions (Schindler et al. 2015) and low in other regions for daily precipitation (Schindler et al. 2015). For seasonal mean temperature, CIV is low for the lower latitudes of North America and high for the higher latitudes, but CIV of seasonal mean precipitation is higher in all the regions except for the middle part of North America (Deser et al. 2012b). Fourth, CIV differs according to the probabilistic index of interest. For example, CIV of daily maximum precipitation corresponding to a 20-year return period is larger than that corresponding to a 10-year return period (Aalbers et al. 2017). In addition, CIV of precipitation extremes, such as daily maximum precipitation, is higher than that of precipitation means (Fischer and Knutti 2014; Fischer et al. 2014).

Most previous examinations of CIV were performed at global or regional scales (Deser et al. 2012a, b, 2014, 2016; Fischer et al. 2014; Thompson et al. 2015; Aalbers et al. 2017; Monerie et al. 2017; Martel et al. 2018; Wang et al. 2018) and daily or monthly temporal scales (Deser et al. 2012a, b, 2014; Fischer et al. 2014; Dai and Bloecker 2018; Martel et al. 2018). Only a few studies have been quantified CIV at smaller and finer scales (Fatichi et al. 2011, 2013; Bengtsson and Hodges 2018; Peleg et al. 2019).

In this study, we use a weather generator to generate various climate realizations simulated at an hourly scale for four different periods: control (CTL), early (ERY), middle (MID), and end (END) periods. South Korea, which is part of the Far East Asia Monsoon region, was selected as a study domain (see SM.1. and Fig. S1) because of its complex rainfall characteristics and distinct seasonal patterns, both temporally and spatially (Kim et al. 2019). Historical and numerical climate data were collected to estimate the parameters of a weather generator. Climatological mean (CM) and CIV were then computed for indices from 40 gauge stations on different temporal scales, representing rainfall volume, maxima, and occurrence in the future and control periods. To assess temporal changes of CM and CIV values between the future periods and the control period, a factor of change (FOC) and a significance test (t -test) were applied. The impact of different representative concentration pathways (RCP 4.5 and RCP 8.5) on CM and CIV was also investigated for all locations and months.

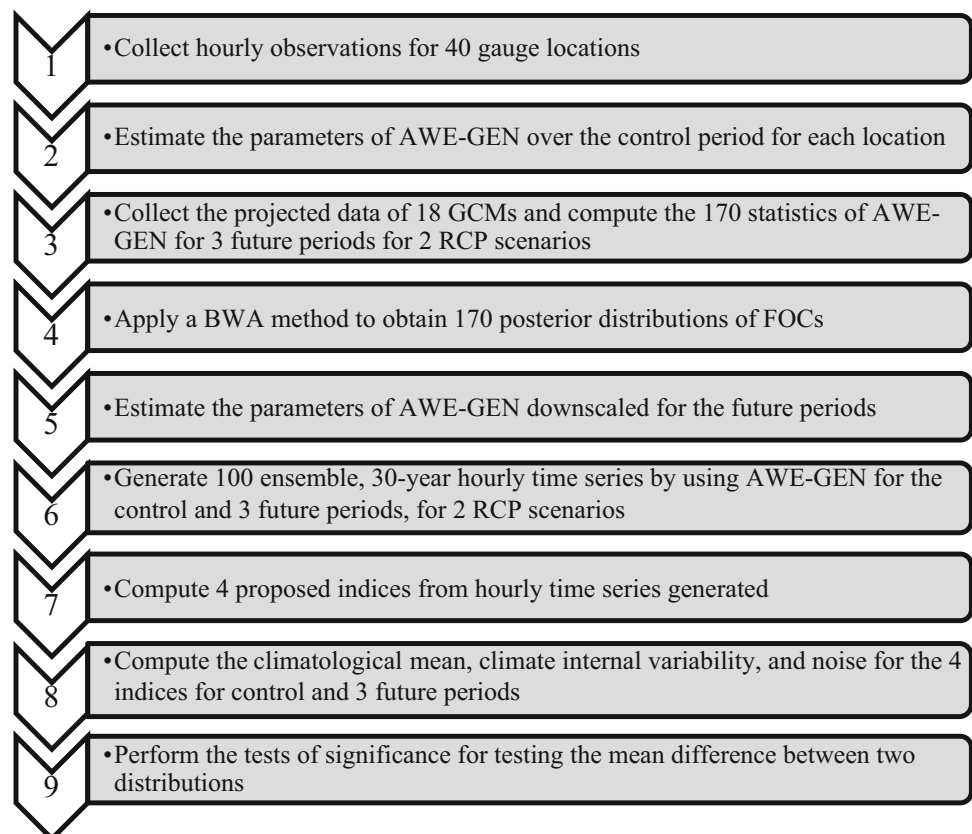
2 Methodology of future CIV estimation

How future climate information is downscaled, how hourly ensemble members of weather variables are generated, and how CIV is quantified is briefly described in the following paragraphs, referring to a flow chart illustrated in Fig. 1.

1. The first step was to collect the time series of meteorological variables at gauge locations of interest. These data should be observed hourly to be used as an input for a stochastic model. They were obtained from an automatic weather observation station operated by the Korea Meteorological Administration as part of the Automated Surface Observing System (<https://data.kma.go.kr/data/grnd/selectAsosList.do?pgmNo=34>). In total, 40 meteorological stations were selected according to the availability of at least 30 years of hourly records. The original data were examined before use and any inappropriate values were removed to avoid potential errors (Kim et al. 2018).
2. Hourly observations were then employed to estimate the present parameters of a stochastic weather generator, the Advanced Weather GENERator (AWE-GEN) (Ivanov et al. 2007; Fatichi et al. 2011). The AWE-GEN was chosen because of the availability of climate information downscaled at finer scales, the ability to

efficiently generate large numbers of ensembles, and the performance of estimating CIV (see SM.2. and Fig. S2). A built-in module for generating precipitation time series consisted of two submodels of the Neyman–Scott Rectangular Pulse (NSRP) model and the autoregressive model, which were adopted for reproducing the high- and low-frequency characteristics of rainfall, respectively. Six parameters of the Poisson, the geometrical, the exponential, and the gamma distributions are employed in NSRP to generate the internal structure of precipitation: the storm time origin, a random number of cells generated for each storm, the cell displacement from the storm origin, and the life time and the intensity of a rectangular pulse associated with each precipitation cell. The parameters are estimated for each month from using an objective function including various statistical properties of precipitation at four different aggregation time scales of 1, 6, 24 and 72 h. The inter-annual variability of precipitation is also simulated using an autoregressive order one model, AR(1), with the skewness modified through the Wilson–Hilferty transformation (Wilson and Hilferty 1931). The AR model consists of four parameters of the average annual precipitation, the standard deviation, the lag-1 autocorrelation, and the random deviate of the process, which are determined

Fig. 1 Flow chart of the adopted procedure and methodology



- from annual observations. More detailed information of submodels and parameters is supplied in a study by Fatichi et al. (2011).
3. Regarding the collection of projected data of global climate models (GCMs), 18 GCMs from the fifth phase of the Coupled Model Model Intercomparison Project (CMIP5) were chosen because they contain consistent daily precipitation data for all time periods and maintain mutual independence among these models. A wide range of statistics (mean, variance, skewness, and frequency of non-precipitation) were then calculated at four aggregation intervals (i.e., 24, 48, 72 and 96 h) for various temporal scales (monthly and annually) over four time periods of “control” (1961–1990) and three future (ERY: 2011–2040; MID: 2041–2070; END: 2071–2100) periods, respectively. RCP 4.5 and RCP 8.5 were used to mimic different emission scenarios. More detailed information on the statistics used is available in Kim et al. (2016b).
 4. The numerical outcomes projected from each GCM generally do not provide any consistency at local and finer scales because of differing spatial resolutions and varying degrees of understanding the physics. Selecting a GCM at random to evaluate climate change may therefore result in considerable uncertainty and risks with respect to mitigation measures. To avoid this ad hoc selection, Bayesian weighted averaging (BWA) (Tebaldi et al. 2005) was applied with the statistical properties of 18 GCMs and observations. BWA can quantify the potential uncertainty in each GCM. A Markov Chain Monte Carlo (MCMC) simulation was used to estimate marginal posterior distributions of the FOCs for the 170 statistics. The latter FOCs were computed in a “product” type (i.e., dividing future statistics by control statistics) for precipitation statistics. More details on BWA parameters, their prior distributions, MCMC algorithm, and burn-in period are summarized in the Step (2) of Kim et al. (2016b).
 5. Because the AWE-GEN adopts statistical information at aggregated temporal scales of 1, 6, 24, 72 h, it was necessary to downscale the daily precipitation statistics from the CMIP5 databases to a finer hourly scale. A few assumptions and empirical relationships were employed to downscale the mean, variance, skewness, autocorrelation, and frequency of non-precipitation identified at 24, 48, 72 and 96 h aggregation intervals to those at 1, 6, 24, 72 h (Fatichi et al., 2011). By combining the historical parameters estimated from the observations with statistics at finer scales, a new set of precipitation parameters was generated over the three future periods for the two RCP scenarios (Fatichi et al. 2011).
 6. Using the new set of parameters obtained above and the AWE-GEN, a 100-ensemble, 30-year hourly time series was generated for precipitation. Ensemble simulations of AWE-GEN are among the repetitions that represent the stochastic nature of precipitation characteristics; they assume stationary climate conditions given periods of interest. Although AWE-GEN can generate hourly time series for many weather variables (e.g., cloud cover, air temperature, radiation, and wind speed), only precipitation was addressed in this study. The details for estimating parameters and generating weather components are described in a study by Fatichi et al. (2011) and a technical reference can be downloaded at: <https://www.umich.edu/~ivanov/HYDROWIT/Models.html>. Because a larger number of model runs does not significantly increase the accuracy of uncertainty quantification (Kim et al. 2016b; Tran and Kim 2019), 100 stochastic simulations were employed for the control and three future periods. For 40 locations and for seven cases (CTL, ERY45 = ERY + RCP45, ERY85 = ERY + RCP85, MID45 = MID + RCP45, MID85 = MID + RCP85, END45 = END + RCP45, and END85 = END + RCP85), a number of 40×700 ensemble simulations were generated. Each set of 100 simulations was derived from a population with the same climate information (i.e., the same AWE-GEN parameters), indicating that external conditions were controlled equally.
 7. To quantify internal variability with respect to an annual time series, we first computed four proposed indices that may be of interest from the generated hourly time series. The indices chosen in this study are total precipitation (abbreviated as totPr), daily (maxDa) and hourly (maxHr) maximum precipitation, and the number of days without precipitation (nonPr). Seasonal and annual patterns can be identified for these indices in evaluations over each month and the whole year. The number of ensembles for the reconstructed annual 30-year time series for the four indices was therefore 4 (indices) \times 13 (months) \times 40 (locations) \times 7 (periods) \times 100 (realizations).
 8. Given the annual time series (X_{ij}) of the four indices, the first and second moments were computed. We also employed the first moment of the mean over 30 years of the time series and the second moments of internal variability and trend. All moments were evaluated for each ensemble member and then converted to representative values over all the members, that is, CM, CIV, and noise. CM and the CIV referred to the ensemble average of the temporal mean and internal variability computed for one ensemble, i , respectively.

$$CM = \frac{1}{N} \sum_{i=1}^N \left(\frac{1}{T} \sum_{j=1}^T X_{ij} \right) \tag{1}$$

$$CIV = \frac{1}{N} \sum_{i=1}^N \left(\sqrt{\frac{1}{T-1} \sum_{j=1}^T (Re_{ij} - \overline{Re}_i)^2} \right) \tag{2}$$

where i and j indicate the ensemble member and the individual year; N and T are the number of ensemble members and years, respectively. Internal variability was quantified largely by using detrended and differenced methods (Kim et al. 2018). The key in both was to separate the external component (i.e., the forced signal) from the given time series and compute the variability (using standard deviation in this study) of the internal component (i.e., residual). The residual (Re_{ij}) in the detrended and differenced methods was computed in Eqs. (3) and (4), respectively:

$$Re_{ij} = X_{ij} - Fit_{ij} \tag{3}$$

$$Re_{ij} = X_{ij} - \frac{1}{N} \sum_{i=1}^N X_{ij} \tag{4}$$

$$\overline{Re}_i = \frac{1}{T} \sum_{j=1}^T Re_{ij} \tag{5}$$

where Fit_{ij} refers to the values of the fitted linear line with respect to X_{ij} . The two methods differed depending on how the internal component is calculated, but the results were largely consistent (Kim et al. 2018). The detrended method was used throughout this study, which was adopted by many previous studies (Giorgi and Mearns 2002; Moise and Hudson 2008; Zhang and Wang 2013; Frankcombe et al. 2015).

The noise, spread around the ensemble mean of model simulations, was computed in two ways by using the trend (“noise1”) and adopting the concept of internal variance (“noise2”) (Kang and Shukla 2006). Regarding the calculations for the trend, it was generally estimated by two approaches. The first approach used the first order of linear regression model to obtain a fitted line over a temporal period (e.g., 30 years) for each ensemble member (Moise and Hudson 2008; Zhang and Wang 2013; Frankcombe et al. 2015). The trend ($trend_i$) for each ensemble member is determined as the vertical difference between the first and last point of the fitted line. Depending on time series, the value of the trend could be negative or positive, representing a decrease or increase, respectively. The trend in the second approach can be estimated by the epoch difference between the temporal means of two time windows (e.g., the first and the last 10 years) (Barnes and Barnes 2015). In this study, the first approach was applied to

estimate the trend of time series within 30 years. Using the set of trends, the noise (“noise1”) was estimated by taking the standard deviation of the trends (Deser et al. 2012a, b, 2014) as:

$$noise1 = \sqrt{\frac{1}{N-1} \sum_{i=1}^N (trend_i - \overline{trend})^2} \tag{6}$$

$$\overline{trend} = \frac{1}{N} \sum_{i=1}^N trend_i \tag{7}$$

The “noise2” was defined as the temporal and ensemble average of the sum of the squared difference between the ensemble member and ensemble mean (Kang and Shukla 2006). This method appeared to be similar to the differenced method.

$$noise2 = \sqrt{\frac{1}{T(N-1)} \sum_{j=1}^T \sum_{i=1}^N (X_{ij} - \overline{X}_j)^2} \tag{8}$$

$$\overline{X}_j = \frac{1}{N} \sum_{i=1}^N X_{ij}. \tag{9}$$

For each location, control, and future period, the CM, CIV, and noise were computed for the four proposed indices of totPr, maxDa, maxHr, and nonPr.

9. Because the ensemble of the temporal mean, internal variability, and trend consisted of 100 values that formed a distribution, we investigated how two distributions corresponding to the control and future periods differed from each other. Tests of significance with a significance level of 0.05 were implemented with the ensemble. A t -test of testing the mean difference of two independent samples was applied to the ensemble of the mean and IV (Von Storch and Zwiers 2001). The null hypothesis was that there is no change in the mean of the distributions, and the alternative hypothesis was that there is a certain difference.

3 Results and discussions

3.1 Comparison of CIV and noise estimations

The methodologies of CIV and noise calculations presented in the previous section measure inter- and intra-ensemble member spreads. Although details for the calculations are not unique, the correlation between these values was expected to be high. Figure 2 compares the results of CIV estimates computed by the detrended method and those of noise estimates computed by the two approaches. For the index of totPr computed monthly and

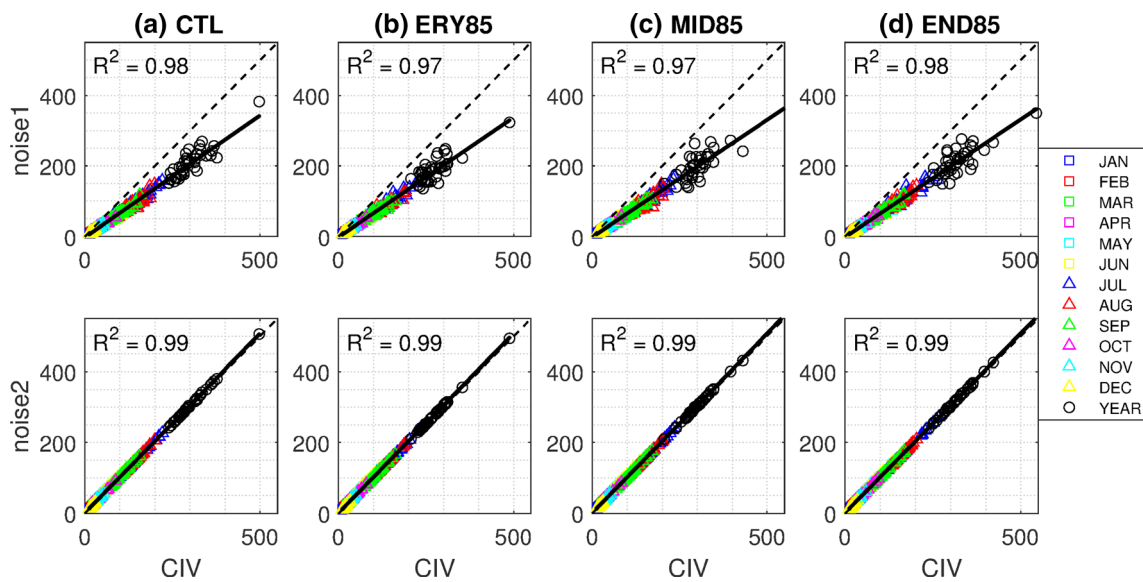


Fig. 2 Comparison between CIV computed by the “detrended” approach and noise computed by two approaches for totPr with RCP85. Each subplot includes the data point of 520 = 40 (locations) times 13 (12 months + year)

annually over 40 locations, the coefficient of determination (R^2) ranged from 0.97 to 0.98 for the first approach of noise (noise1) and was approximately 0.99 for the second approach of noise (noise2) over future periods. These high R^2 values confirmed a high correlation between the values of CIV and noise, and that the methodologies presented for quantifying the variability are seamless. The same conclusions can be drawn for other indices (see Figs. S1–S3).

Although the correlation between CIV and noise was high in the above figures, the results in all time series that do not eliminate the effects of external forcing were not always correlated. The reason for a high correlation is that the ensemble of the precipitation time series used was generated under a stochastically stationary climate condition in which the external components were removed. If such a calculation was applied to natural time series, there would be a correlation between climate total variability and noise calculations, but a correlation between CIV and noise cannot be guaranteed.

3.2 Estimation of climatological mean and its future change

The CM of annual total precipitation ranged from 1011.78 to 1838.49 mm (1307.57 mm in average) for 40 locations in the CTL period (Fig. 3; Table 1). These values significantly increased in the END period for RCP 8.5, with an average value of up to 1484.98 mm and minimum and

maximum values of 1187.60 and 1955.47 mm, respectively. Similarly, when examining CM values for maxDa and maxHr, an overall increase for these extreme indicators can be seen as the period goes on. The difference in CM values by local location almost doubled. The spatial average in South Korea for CM values increased in the END85 period compared with CTL by 13.56, 16.75 and 17.85% for totPr, maxDa, and maxHr, respectively. However, the overall trend in CM values for nonPr was different. The number of days of no rain in a year was comparable to the CTL period in most future cases, regardless of climate change. CM values vary by location from month to month. Table 1 provides exact numbers for the mean and extreme indices.

As well as these nationally averaged statistics, national distributions and patterns tended to be quite dissimilar depending on the index. To divide the locations into distinctive zones, a *K*-means cluster algorithm was applied to the CM values, and four clusters ($K = 4$) were chosen according to the Elbow method (Kim et al. 2018). For the indices of totPr and maxDa, regions with higher CM values (light red and red circles in Fig. 3) were mostly located at the northern areas and the southern coastal regions of South Korea, while those with lower CM values (blue circles) were in the central part. In the case of maxHr, locations adjacent to the western coast were included as the areas showing higher CM values, while only the central inland area corresponded to the areas with lower CM values. For

nonPr, the spatial distribution of the CM values was relatively homogeneous. Almost similar spatial patterns were observed for all indices in RCP 4.5 (see Fig. S6).

Although locations with high or low CM values could be identified, it was still difficult to determine how much the CM values for each location will change in the future. As our main concern was how CM will change, the FOC were calculated as the product type and shown in Fig. 4. As a result of examining the FOC value for totPr, FOC had a comparable range, from 0.98 to 1.06, for 40 locations in the nearest future period, but the FOC value in the farthest future period was much larger, from 1.06 to 1.22 (Table 2). The latter number means that annual mean precipitation can increase up to 22% in some locations. The spatial averages of the 40 FOCs were 1.02, 1.08, and 1.14 for the ERY85, MID85, and END85 periods, and 1.01, 1.05 and 1.09 for the ERY45, MID45, and END45 periods, respectively. Likewise, when examining the FOC of maxDa and maxHr, it was predicted that the maximum precipitation values will also increase in the future, although there was a difference in their size. The FOC of nonPr showed a value close to 1.0 throughout all the future periods.

Similarly, spatial distributions and patterns tend to differ depending on the index. For totPr, a spatial homogeneity was found for most of the domain for FOC of CM; but relatively small FOC values were found in the southern region in the END85 period. Regarding maxDa and maxHr, the FOC values of the middle region were relatively large, but the overall tendency was not remarkable. For nonPr, large circles were mostly located in the central inland regions of South Korea, while small circles were distributed in the southern coastal regions. Spatial similarities were also observed for FOCs of RCP 4.5 with changes in circle size (see Fig. S7).

We attempted to calculate FOCs for each location, but needed to perform a *t*-test to investigate if two distributions of the temporal mean values and the future changes in two ensemble mean values (i.e., CM) were statistically significant. It was straightforward to judge whether a future change in CM is significant because was colored red, as in Fig. 4 and Fig. S7. Although there was no significance at

Fig. 4 Spatial distribution of FOCs of the CM values for the whole year with RCP85. The FOC is computed as the ratio, by dividing future CM values by control CM values for each station for 4 indices. The size of circles represents the magnitude of FOCs. A significant *t*-test is applied to 2 distributions of IV in the future and control periods for each location. The green color means that there is no difference between 2 distributions; while red color refers that those are significantly different

few locations, future CM values changed significantly at most locations.

3.3 Estimation of CIV and its future change

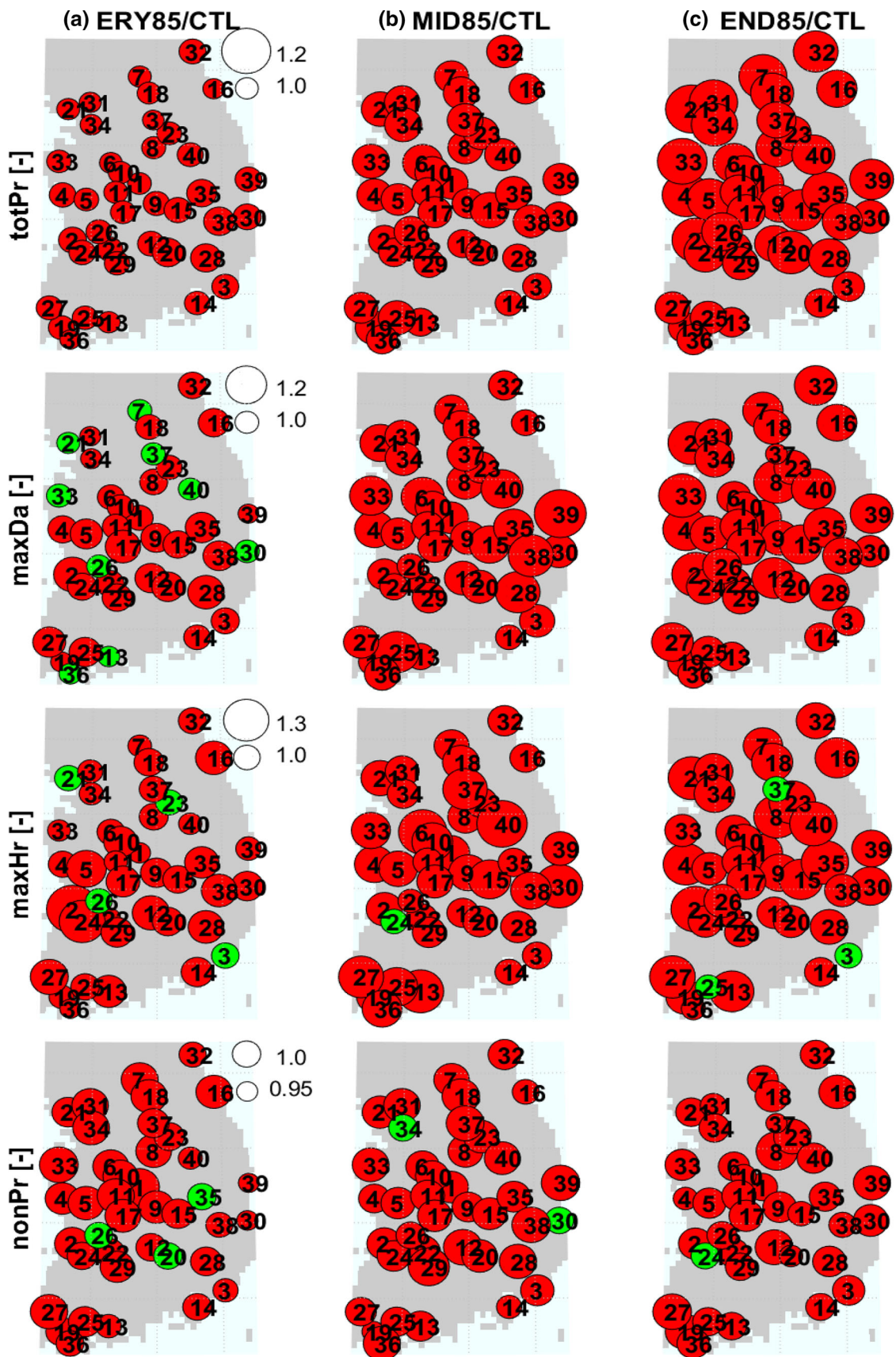
Various properties of CIV are illustrated in this section: (1) spatial estimates of CIVs over South Korea, (2) spatial distribution of FOCs of the CIV values for 40 locations in the future periods compared with the control period, and (3) effects of two representative concentration pathways (RCP 4.5 and RCP 8.5). First, spatial patterns of CIV over South Korea are displayed with varying CIV values, depending on many factors (i.e., indices, emission scenarios, and seasons). The CIV of totPr ranged from 239.77 to 497.46 mm (300.52 mm on average) over 40 locations in the CTL period. These values decreased slightly in the ERY85 period, with an average value of 271.31 mm before increasing in the MID85 and END85 periods to 305.91 and 319.28 mm, respectively (Fig. 5; Table 3). When investigating the CIV values for maxDa and maxHr, an overall

Table 2 The minimum, maximum of FOCs of CM values over the 40 locations, which are computed for the whole year

	totPr (–)	maxDa (–)	maxHr (–)	nonPr (–)
ERY45/CTL	0.98–1.04	0.97–1.32	0.88–1.50	1.00–1.04
MID45/CTL	1.01–1.08	0.98–1.22	0.90–1.26	0.98–1.03
END45/CTL	1.03–1.13	1.00–1.41	0.89–1.45	0.98–1.02
ERY85/CTL	0.98–1.06	0.96–1.16	0.90–1.41	0.98–1.03
MID85/CTL	1.04–1.13	1.04–1.33	0.98–1.38	0.98–1.04
END85/CTL	1.06–1.22	0.98–1.22	0.95–1.37	0.98–1.04

Table 1 The minimum, maximum of CM values over the 40 locations, which are computed for the whole year

	totPr (mm)	maxDa (mm)	maxHr (mm)	nonPr (day)
CTL	1011.78–1838.49	94.79–185.70	25.76–49.98	270.8–295.57
ERY45	1051.09–1868.02	100.04–196.01	28.67–63.22	275.87–299.74
MID45	1095.19–1858.34	100.65–201.77	26.9–53.63	269.51–302.10
END45	1131.64–1974.60	111.00–191.75	30.56–61.08	270.98–299.49
ERY85	1066.08–1874.08	101.15–192.31	27.68–51.19	270.52–295.87
MID85	1114.43–1905.17	112.81–200.40	30.42–58.97	271.39–302.20
END85	1187.6–1955.47	115.04–207.14	31.47–55.37	271.77–301.13



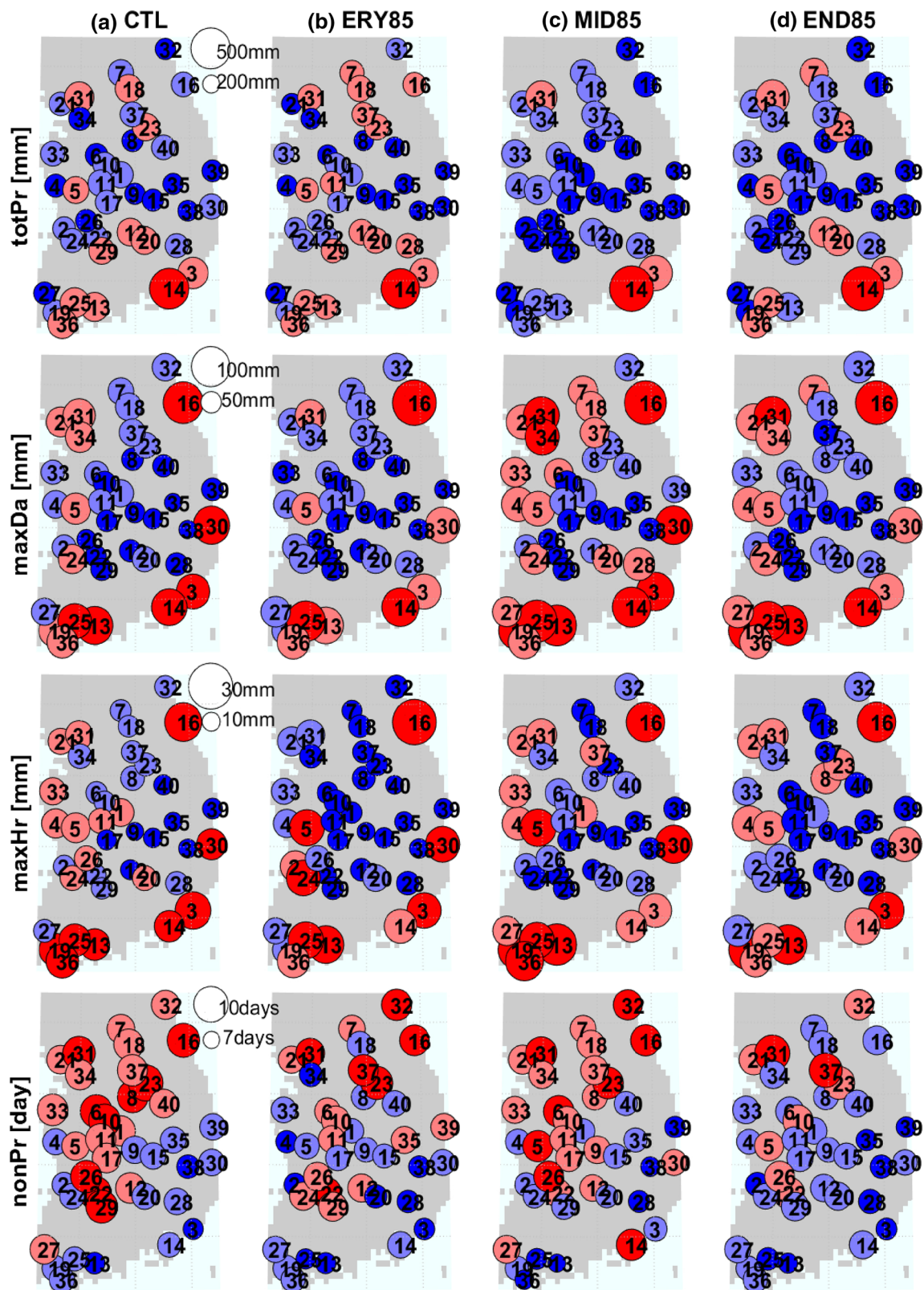


Fig. 5 Spatial distribution of CIV values over South Korea in the control and 3 future periods (ERY, MID, END) with the RCP85 scenario for 4 legends computed for the whole year. 40 locations are divided into 4 clusters (colored circles from blue (the smallest

cluster), light blue, light red to red (the largest one)) by using the *K*-means algorithm. The number near white circles are used as legends to indicate the relative magnitudes of circle size

Table 3 The minimum, maximum of CIV values over the 40 locations, which are computed for the whole year

	totPr (mm)	maxDa (mm)	maxHr (mm)	nonPr (day)
CTL	239.77–497.46	41.24–105.00	9.47–24.66	7.59–10.02
ERY45	183.82–464.34	40.92–115.34	9.89–28.14	6.68–9.73
MID45	229.75–466.87	43.23–119.80	9.03–29.72	7.55–9.86
END45	216.41–629.85	48.30–105.37	10.14–28.67	7.36–9.70
ERY85	206.68–487.79	43.24–115.28	9.51–29.71	7.50–9.55
MID85	205.84–558.75	48.07–110.47	11.35–26.48	7.16–9.52
END85	238.10–544.28	48.61–110.10	10.80–25.83	7.47–10.10

increase was evident for the future periods. The spatially averaged CIV values in the END85 period increased by approximately 6.2, 13.7 and 16.8% for totPr, maxDa, and maxHr, respectively, compared with the values in the CTL period. For nonPr, there was little change in CIV values in all periods and locations. The spatially averaged CIV values in the END85 period decreased by 3.15%. More details are provided in Table 3 for CIVs computed annually, and the numbers for RCP 8.5 correspond to the 16 sub-plots of Fig. 5. Although no increasing or decreasing trends were evident for the minimum and maximum values among periods, the spatially averaged values for totPr, maxDa, and maxHr exhibited an increasing trend, with a decreasing trend for nonPr.

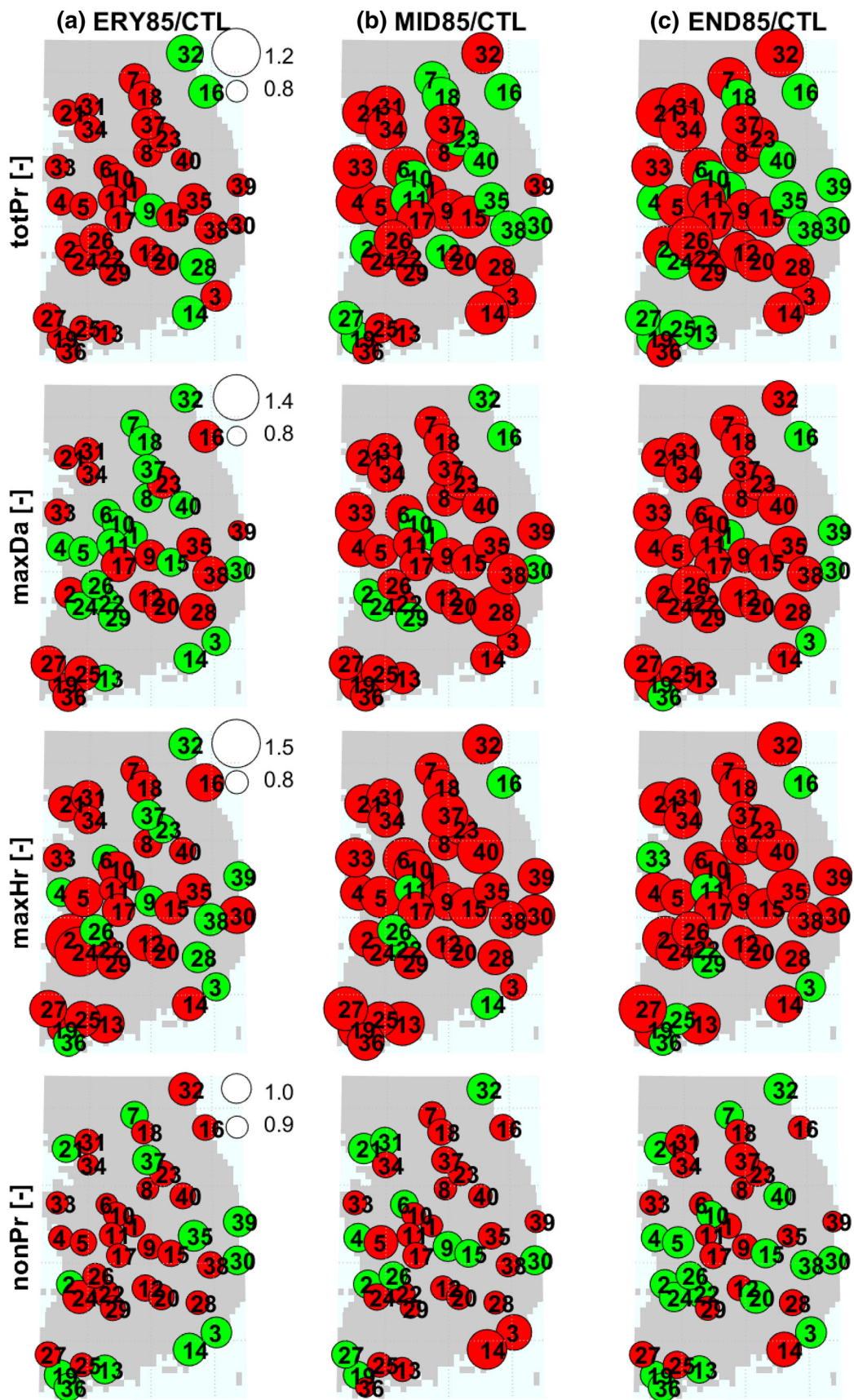
The spatial distribution of CIV was not identical to that of CM. For totPr, higher CIV values were found in the southern coastal region of the country. For maxDa and maxHr, large CIV values were concentrated on three coasts, i.e., west, south, and east, while relatively small CIV values were located in the central inland region. For nonPr, higher CIV values were found in northern and western areas. For RCP 4.5, Fig. S8 shows no significant differences compared with spatial distributions in Fig. 5.

Some locations that are close to each other shared similar CM values but had different CIV values. For example, in August of END85, the CM values for totPr in Pohang (No. 30) and Youngcheon (No. 38), which are approximately 40 km apart, were nearly similar (257.24 and 257.51 mm), but the CIV values were different (136.21 and 107.47 mm). Therefore, even if the climate information of one location is perfectly known, it is risky to regionalize it to a nearby location.

The ratio of CIVs for totPr between the control and future periods ranged from 0.77 to 1.03 (0.9 on average) for 40 locations in the ERY period with RCP 8.5 (Fig. 6;

Table 4). These values increased in the END85 period with an average of up to 1.06 with minimum and maximum values of 0.96 and 1.22, respectively. For maxDa and maxHr, the same increasing pattern over periods can be observed for the spatial averages. For example, from 1.02 to 1.15 at ERY85 and END85 periods for maxDa, and from 1.05 to 1.18 for maxHr. Regarding nonPr, they were not significantly different for locations and periods, respectively, which is consistent with the other results presented above the figures. The outcomes of the *t*-test are somewhat different from the future changes in CM, for which there was a clear message for almost all locations and periods. The significance of future changes in CIV was not confirmed at many locations, and this was more prominent in RCP 4.5 (see Fig. S9).

Because Figs. 4 and 6 show the results of indices calculated over the whole year, the seasonal variability of CM and CIV was not represented. It is possible to quantify how CM and CIV values will change considering seasonality in the future and how large the changes will be. Figures 7 and 8 illustrate nonparametric kernel distributions for the FOCs of CM and CIV values calculated monthly and annually. The number of samples is 520, and consists of 40 locations and 13 cases (12 months plus the whole year). If the ratios on the *x*-axis were greater than 1, the future value was greater than the control value. The first and second moments of the distributions can be an aggregated indicator of future changes for all locations and for all months. It was clearly seen that both CM and CIV increase in future for totPr, maxDa, and maxHr, except for nonPr, and this tendency becomes prominent in the future. For instance, regarding totPr for END85, CM and CIV values in the future were 14.2 and 16.5% greater than those in the control period (see Figs. 7 and 8 for mean and standard deviation). For nonPr, no significant



◀**Fig. 6** Spatial distribution of FOCs of the CIV values for the whole year with RCP85. The FOC is computed as the ratio, by dividing future CIV values by control CIV values for each station for 4 indices. The size of circles represents the magnitude of FOCs. A significant *t*-test is applied to 2 distributions of IV in the future and control periods for each location. The green color means that there is no difference between 2 distributions; while red color refers that those are significantly different

Table 4 The minimum, maximum of FOCs of CIV values over the 40 locations, which are computed for the whole year

	totPr (–)	maxDa (–)	maxHr (–)	nonPr (–)
ERY45/CTL	0.73–1.01	0.87–1.32	0.70–1.53	0.86–1.05
MID45/CTL	0.91–1.12	0.92–1.29	0.78–1.47	0.92–1.05
END45/CTL	0.86–1.27	0.90–1.39	0.82–1.64	0.92–1.14
ERY85/CTL	0.77–1.03	0.81–1.19	0.71–1.53	0.89–1.05
MID85/CTL	0.81–1.15	0.93–1.49	0.89–1.43	0.87–1.13
END85/CTL	0.96–1.22	0.93–1.29	0.91–1.49	0.88–1.06

change was seen among periods, e.g., for END85, a 1.0% increase for CM and a 1.8% decrease for CIV. As expected, these first and second moments (summarized in Tables S1 and S2) were smaller for RCP 4.5 (see Figs. S10 and S11).

The impact of different RCPs (4.5 and 8.5) on CM and CIV values was investigated. A similar analysis of the probabilistic distributions for the RCP comparison presented made in Fig. 9 and Table S3, with the same sample size of 520. The CIV values of RCP 8.5 were sometimes larger or smaller than those in RCP 4.5. The relative difference between the two emission scenarios reached 10% for totPr, maxDa, and maxHr, while for nonPr, there was almost no difference between the scenarios (approximately 1%). Among these distributions, not only the mean but also the standard deviation were shown to be the greatest for maxHr among indices. Regarding CM, a similar pattern can be seen overall, although the RCP difference is smaller than that in CIV (see Fig. S12 and Table S4). For example, the RCP difference is indicated as 8.1% for maxHr.

Some studies show that the intrinsic variability of extreme precipitation is larger than that of mean precipitation (Fischer and Knutti 2014; Fischer et al. 2014). Consistent with previous studies, the degree of perturbation in CIV compared with CM was higher in maxDa and maxHr than in totPr. These ratios were higher, at 0.48 and

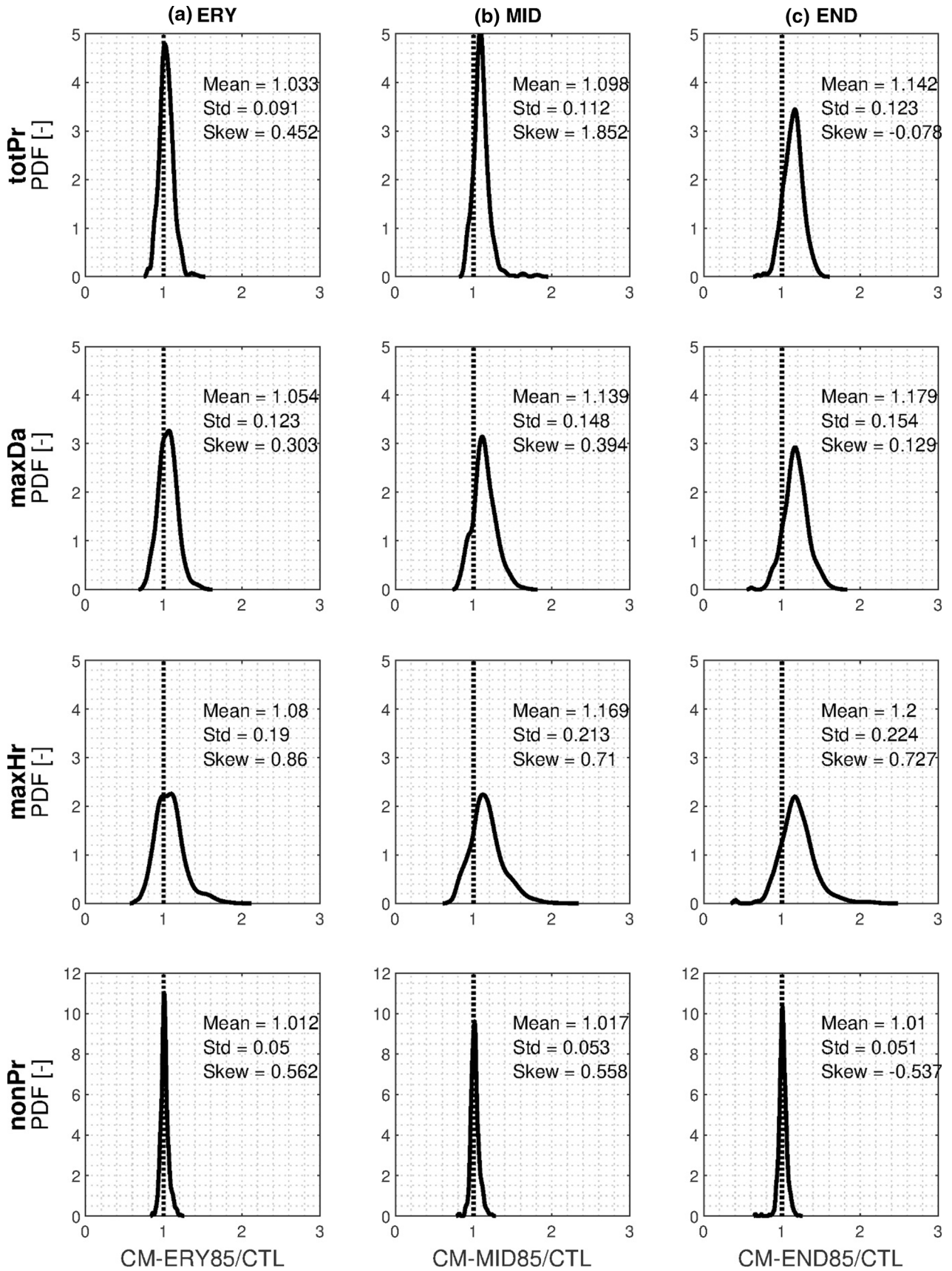
0.40, for maxDa and maxHr than 0.22 for totPr in the END85 period (see Tables 1 and 3).

3.4 Inference of CIV future change from CM change

Because extensive efforts in previous studies have been made regarding the future change of CM, the future change of CIV can be assessed by exploring how the FOC of CIV is related to the FOC of CM in future periods. Once we identified the relationship, we could readily infer the FOC of CIV even if we only had the information on CM. Figure 10 shows the results of comparisons between the FOCs of CM and FOCs of CIV for four indices. The results using all the data addressed in this study show that the two comparing variables are positively correlated to the three precipitation ‘quantity’ indices of totPr, maxDa, and maxHr while negatively (or not) correlated to the precipitation ‘occurrence’ index of nonPr. This implies that if the future CM is expected to increase, it can be inferred that the future CIV will also increase—this tendency is even more pronounced for the two extreme indices of maxDa and maxHr (see the high values of the coefficient of determination). In contrast, regarding the nonPr which behaves differently with the tendency of other precipitation ‘quantity’ indices, we infer that the climate internal variability in the total number of dry days would be unlikely influenced by whether its magnitude increases or decreases in the future. Even if there is no increase or decrease in future CM values, the change in future CIV values is significant. That is, even if the values of the FOC of CM are near 1 (the total number of dry days would be likely unchanged in the future), the FOC of CIV values vary from 0.5 to 2.5 (the significant variation of dry days would have occurred in some months and locations). The same conclusions can be also drawn for the six different periods considered (not shown).

3.5 Inference of future extremes from future total precipitation

It is meaningful to infer the magnitude (CM) and variability (CIV) of future extreme precipitation from those of future total precipitation. Figure 11a–d show pairwise comparisons of FOCs for the pairs of maxDa and totPr and maxHr and totPr for CM and CIV in the END period of RCP85. Samples for 40 locations and 13 cases (12 months and the whole year) are illustrated. First,



◀ **Fig. 7** Non-parametric kernel distributions for the FOCs of CM values between the control and 3 future periods for RCP85: **a** ERY, **b** MID and **c** END. Each row plots correspond to indices of totPr, maxDa, maxHr, and nonPr, respectively. The number of samples used for making distributions is 520, i.e., 40 (locations) times 13 (12 months + year)

looking at the range of FOC values in these subplots, the range of FOCs of CIVs is greater than that of FOCs of CMs; the range corresponding to the maximum precipitation indices (i.e., maxDa and maxHr) is greater than that corresponding to the total precipitation index (i.e., totPr); and the range of hourly maximum precipitation (i.e., maxHr) is greater than that of daily maximum (i.e., maxDa). It is also noteworthy that the minimum of their ranges is similar in all the cases, but the maximum is different. That is, the extent to which the future index is larger (or smaller) than the present index is more pronounced at the precipitation extreme than the volume, and the extreme at the finer temporal scale may be more pronounced among the extremes.

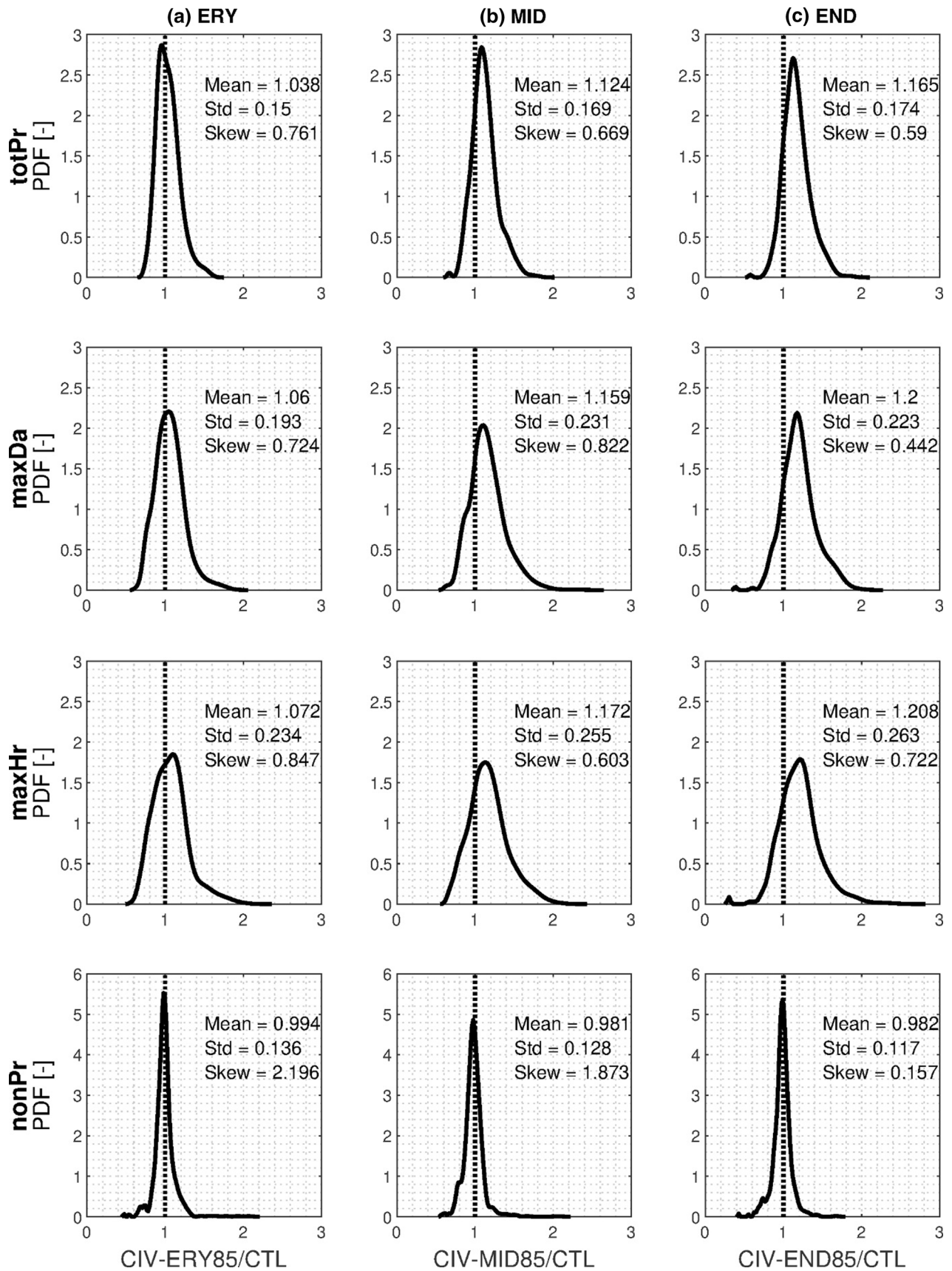
This tendency can easily be seen by calculating the FOC ratios of the maximum indices to the total index. Probabilistic distributions made from the 520 samples of the comparisons using a nonparametric kernel distribution are also shown in Fig. 11e. Most of the sample data are located in the center of these distributions, and the first moments of these distributions are slightly greater than 1—it ranges from 1.03 to 1.05. The statement that these ratios are close to 1 means that the pairs of FOCs are located close to the 1:1 line in Fig. 11a–d. In contrast, the large quantities of sample data also remain in both tails of the distributions. The minimum and maximum ranges of the ratios are [0.54–1.37], [0.36–1.85], [0.67–1.36], and [0.40–2.08] for blue, red, green, and magenta lines, respectively. The presence of ratio values on both tails means that the pairs of FOCs are significantly off the 1:1 line. For example, the following question can be answered: if interannual variability (or mean, i.e., CIV or CM) in total precipitation increases by 20% in the future, will the variability in extreme rainfall increase by 20% in the future? Yes, if the ratio corresponding to some months and locations to be examined is close to 1:1 line; No, if it is far from the line. The information of tails ultimately indicates that future changes in total and extreme precipitation are likely to be

decoupled for some months or at some locations. Moreover, the tail for the distributions of the ratio between FOCs of maxHr and totPr is longer and heavier than for those of maxDa and totPr. In other words, this heavy-tailed tendency is more noticeable on the hourly scale than the daily scale. It is therefore important to investigate the characteristics of sample distributions at different temporal scales, i.e., higher moments (tails) as well as the first moment of distribution (Kim et al. 2016a, c).

3.6 Inference of CIV spatial variability from season

While the land is very small, the climate of the Korean peninsula is characterized by severe climate differences, and significant seasonal patterns are annually repeated. Noticeable seasonal variations of (monthly and annual) CIV values of 40 locations for all indices are well observed (see Fig. S13). It can be seen that the CIVs of 40 locations were high during the summer season (from July to September) and low during the winter (from December to February). How then do regional deviations of CIV appear? Is the spatial deviation of CIV larger during summer when CIVs are spatially larger? The coefficient of determination (R^2) in Fig. 12 provide a possible answer to this question. If data points fit perfectly on a linear line (i.e., $R^2 = 1.0$), spatial mean and the spatial variability are completely correlated. The totPr and maxDa result meet this description. If the CIVs are spatially is small in winter (i.e., smaller mean), the spatial variability of CIVs will also be small (i.e., homogeneous), whereas in summer when the CIVs are large (i.e., larger mean), the spatial distribution of CIVs will be heterogeneous as well. However, in the indices of maxHr and nonPr, this tendency cannot be guaranteed: even in summer, its spatial distribution may be homogeneous or heterogeneous.

Another interesting feature in the rainy monsoon season from July to September in South Korea is that the spatial pattern showing higher CIVs differed according to the indices (see Fig. S14–S16). In terms of rainfall amount-related indexes, July to September all belong to the rainy season, but the spatial distribution of CIV is locally different. For example, in July, the CIV of the central region is large due to the longitudinal movement of the *Jangma* front, while in September, the southern and east coasts,



◀**Fig. 8** Non-parametric kernel distributions for the FOCs of CIV values between the control and 3 future periods for RCP85: **a** ERY, **b** MID and **c** END. Each row plots correspond to indices of totPr, maxDa, maxHr, and nonPr, respectively. The number of samples used for making distributions is 520, i.e., 40 (locations) times 13 (12 months + year)

located on the path of typhoons, have relatively large CIVs. On the other hand, during that season, it is a nationwide phenomenon that the *Jangma* front and typhoons affect, so the variation of CIV in dry days across the country is small.

4 Summary and conclusion

This study aimed to quantify and assess CIV as well as CM in future periods using the RCP 4.5 and RCP 8.5 emission scenarios over South Korea. The AWE-GEN was employed to generate 100 ensembles of 30-year hourly time series from 40 meteorological stations. These 100 precipitation series were built under a stochastically stationary climate condition from which external components have been removed. CIV was estimated from the detrended method and compared with the noise computed by two approaches. The number of CIVs (and CMs) addressed in this study is 14,560, i.e., 4 (indices) \times 13 (months) \times 40 (locations) \times 7 (periods). The extremely high value of the coefficient of determination between the values of CIV and noise for all indices indicates that the methodologies adopted to estimate the variability are seamless (Fig. 2 and Figs. S3–S5).

For estimates of CM and CIV, the *K*-means algorithm was applied to classify 40 locations into four groups, and the *t*-test was employed to identify whether their estimates for the control and future periods were statistically different. Spatial distribution of locations indicating higher CM and CIV was found to vary (Figs. 3 and 5), depending on index, periods, emission scenarios, locations, and months. It is widely understood that the national average of CM and CIV will increase in the future, and that the increase will be greater in the RCP 8.5 and END periods. However, the results of *t*-test show that future change of CM is observed for almost all the locations of South Korea, while future change of CIV was not confirmed at many locations (Figs. 4 and 6).

The nature of future changes in CM and CIV according to the indices of interest is notable. The characteristics of

the three precipitation-quantity indices (totPr, maxDa, and maxHr), and the precipitation-occurrence index (nonPr) are largely distinct. Future increases in CM and CIV have been well observed and their spatial distributions are heterogeneous, but in nonPr, future changes are not noticeable and spatial distribution is relatively homogeneous. Non-parametric kernel distributions made from 520 samples corresponding to 40 locations and 13 cases (12 months plus the whole year) illustrate the overall future change of CM and CIV (Figs. 7 and 8). Specifically, CM was observed to increase by 14.2, 17.9 and 20.0% for totPr, max Da, and maxHr, respectively in the END85 period as compared with the CTL period (Table S1), and CIV increases by 14.0, 17.0, and 18.0% (Table 2).

The influence of RCP 4.5 and RCP 8.5 on CM and CIV was also examined for all indices using a nonparametric kernel distribution. The relative difference between two emission scenarios reached 10.0% for CIV and 8.1% for CM in the first three indices, while there was no difference for nonPr (Fig. 9 and Table S3).

If access is available only to CM, it is valuable to infer CIV future change from the CM change. The relationship between FOCs of CIV and CM can help infer the CIV change. The results in Fig. 10 show that the two comparing variables are positively correlated to the three precipitation ‘quantity’ indices of totPr, maxDa, and maxHr while negatively (or not) correlated to the precipitation ‘occurrence’ index of nonPr. This implies that if the future CM is expected to increase, it can be inferred that the future CIV will also increase—this tendency is even more pronounced for the two extreme indices of maxDa and maxHr. In contrast, regarding the nonPr, we infer that the climate internal variability in the total number of dry days would be unlikely influenced by whether its magnitude increases or decreases in the future.

It is meaningful to infer the magnitude (CM) and variability (CIV) of future extreme precipitation from those of future total precipitation. The extent to which the future index is larger (or smaller) than the present index is more pronounced at the precipitation extreme than the volume, and the extreme at the finer temporal scale may be more pronounced among the extremes. The presence of ratio values on both tails in Fig. 11e indicates that the pairs of FOCs are significantly off the 1:1 line. The information of tails ultimately implies that future changes in total and extreme precipitation are likely to be decoupled for some months or at some locations. The degree of decoupling

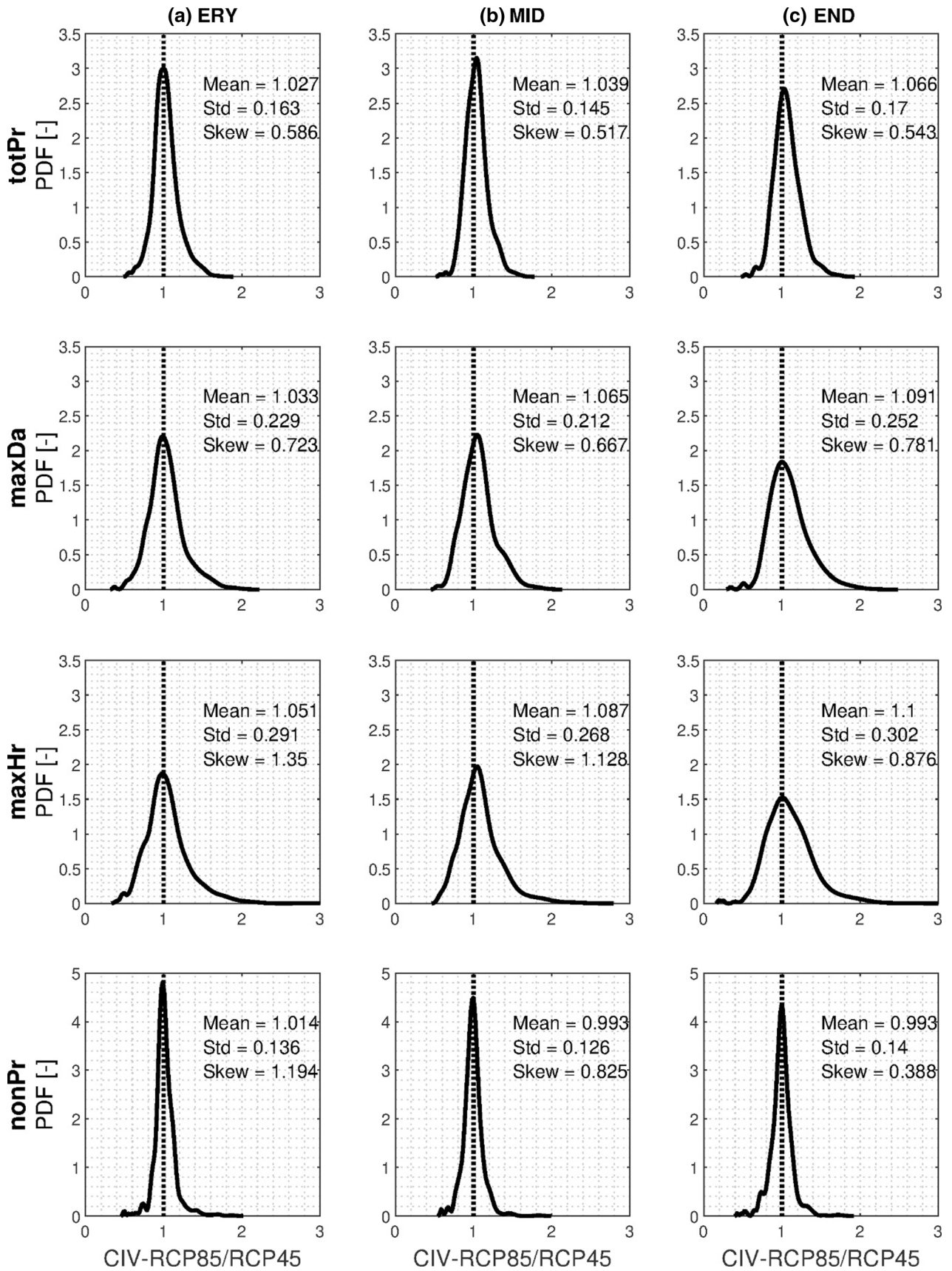


Fig. 9 Non-parametric kernel distributions for the ratio of CIV values between the emission scenarios of RCP45 and RCP85: **a** ERY, **b** MID and **c** END. Each row plots correspond to indices of totPr, maxDa, maxHr, and nonPr, respectively. The number of samples used for making distributions is 520, i.e., 40 (locations) times 13 (12 months + year)

(i.e., heavy-tailed tendency in Fig. 11e) is more noticeable on the hourly than the daily scale. It is therefore important to investigate the characteristics of sample distribution at different temporal scales, i.e., higher moments (tails) as well as the first moment of distribution.

CIV values depend on season (Fig. S13): they were high during the summer (from July to September) and low during the winter (December–February). The question then arises of whether the spatial deviation of CIV is also larger during the summer. High values of the coefficient of determination (R^2) in Fig. 12 could imply that the spatial mean and the spatial variability are largely correlated for totPr and maxDa. If CIV values are small in winter, the spatial variability of CIV will also be small (i.e., homogeneous), whereas in summer when CIV values are large, the spatial distribution of CIV will be heterogeneous as well. However, in the indices of maxHr and nonPr, this

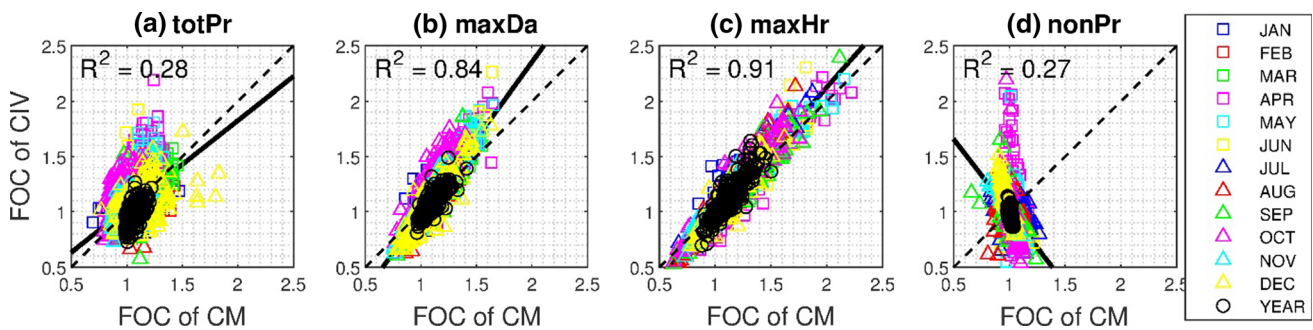


Fig. 10 Comparisons between FOCs of CM and FOCs of CIV for 4 indices. The number of data points is 3,120 for the subplots (40 locations \times 13 (12 months + year) \times 6 comparing periods). The R^2 values are computed for the fitted linear line (i.e., black solid lines)

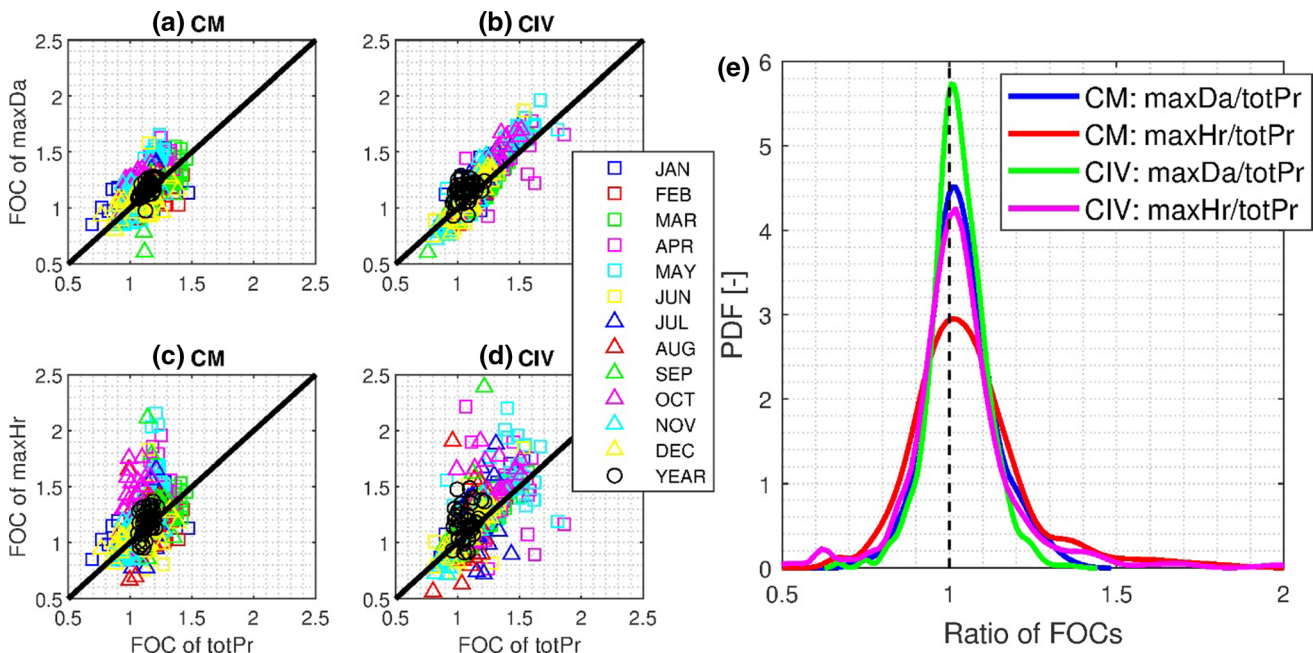


Fig. 11 Pairwise comparisons of FOCs for the pairs of maxDa and totPr, and maxHr and totPr for CM and CIV at END period of RCP85. For each subplot on the left side, 520 data points (40 (locations) times

13 (12 months + year)) are used. The subplot on the right side illustrates the non-parametric kernel distributions for the FOC ratios of the maximum indices to the total index

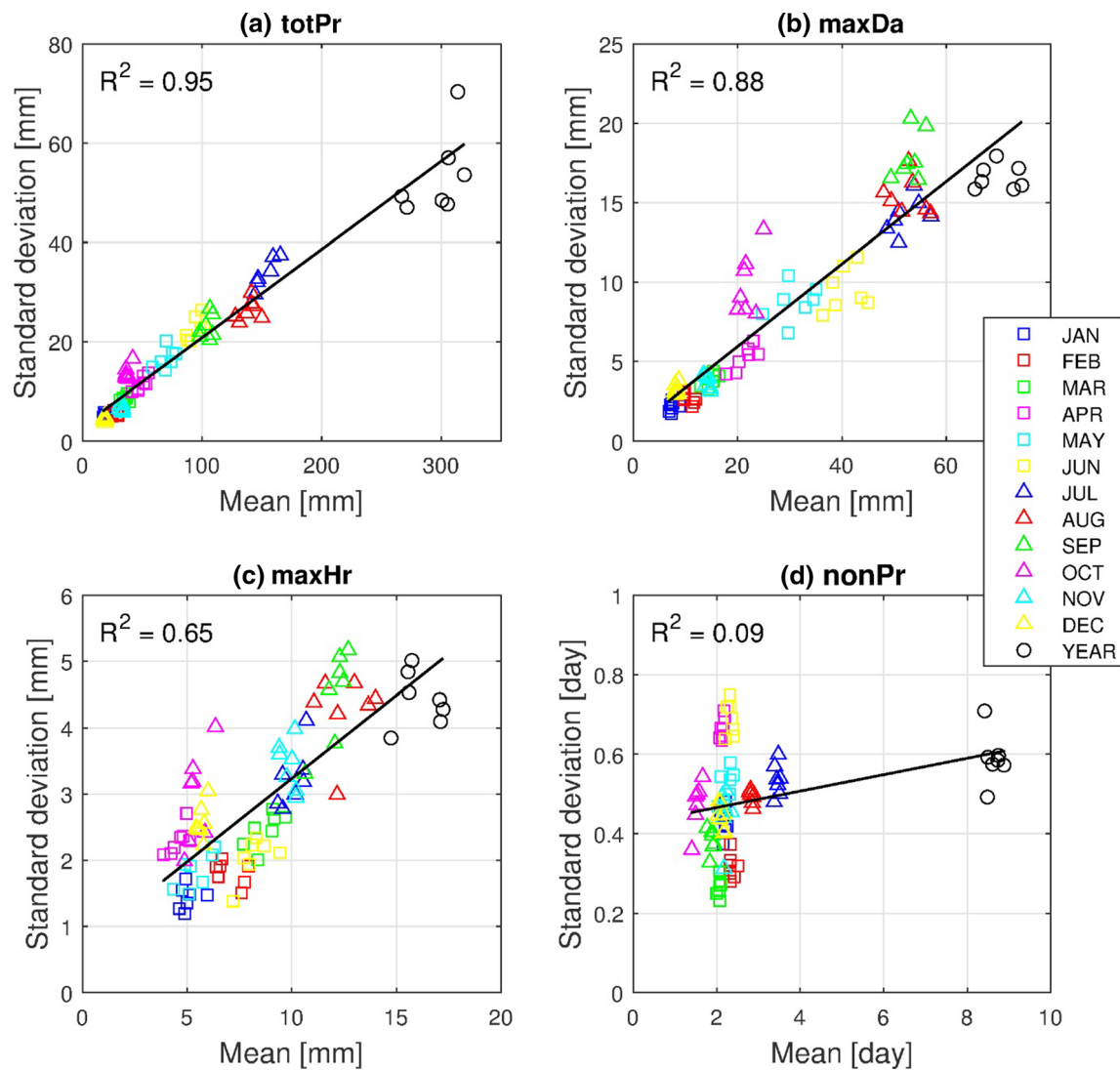


Fig. 12 Spatial mean versus spatial variability (i.e., standard deviation) of FOCs over 40 locations for **a** totPr, **b** maxDa, **c** maxHr and **d** nonPr. The number of samples in each plot is 91, i.e., 7 (periods)

correlation cannot be guaranteed: even in summer, its spatial distribution may be homogeneous or heterogeneous.

Future climate change is likely to involve more shifting trends than seen in the past, and predictions can contain large amounts of uncertainty. Among many uncertainties, we estimated and investigated CIV and CM in future periods at fine temporal scales at a station level. Indeed, some nearby locations shared similar CM values but had

times 13 (12 months + year). The coefficient of determination (R^2) is computed over the fitted black line

diverse CIV values. Because distances between locations can be significant, future research should consider spatial coherence among stations when generating spatiotemporal rainfall time series and computing spatially-varying CM and CIV values. Spatial averages lost locality, and extreme information on various temporal scales could be different. Applying our methodologies to finer scales will help assess

the impact of climate change on uncertainties and develop appropriate adaptation and response strategies.

Acknowledgements This work was supported by the 2020 Research Fund of University of Ulsan.

References

- Aalbers EE, Lenderink G, van Meijgaard E, van den Hurk BJM (2017) Local-scale changes in mean and heavy precipitation in Western Europe, climate change or internal variability? *Clim Dyn* 50(11–12):4745–4766
- Addor N, Fischer EM (2015) The influence of natural variability and interpolation errors on bias characterization in RCM simulations. *J Geophys Res Atmos* 120(19):10180–110195
- Barnes EA, Barnes RJ (2015) Estimating linear trends: simple linear regression versus epoch differences. *J Clim* 28(24):9969–9976
- Bengtsson L, Hodges KI (2018) Can an ensemble climate simulation be used to separate climate change signals from internal unforced variability? *Clim Dyn* 52(5–6):3553–3573
- Dai A, Bloecker CE (2018) Impacts of internal variability on temperature and precipitation trends in large ensemble simulations by two climate models. *Clim Dyn* 52(1–2):289–306
- Deser C, Hurrell JW, Phillips AS (2016) The role of the North Atlantic Oscillation in European climate projections. *Clim Dyn* 49(9–10):3141–3157
- Deser C, Phillips A, Bourdette V, Teng HY (2012a) Uncertainty in climate change projections: the role of internal variability. *Clim Dyn* 38(3–4):527–546
- Deser C, Knutti R, Solomon S, Phillips AS (2012b) Communication of the role of natural variability in future North American climate. *Nat Clim Change* 2(11):775–779
- Deser C, Phillips AS, Alexander MA, Smoliak BV (2014) Projecting North American climate over the next 50 years: uncertainty due to Internal Variability. *J Clim* 27(6):2271–2296
- Domeisen DIV, Badin G, Koszalka IM (2018) How predictable are the arctic and North Atlantic Oscillations? Exploring the variability and predictability of the Northern Hemisphere. *J Clim* 31(3):997–1014
- Fatichi S, Ivanov VY, Caporali E (2011) Simulation of future climate scenarios with a weather generator. *Adv Water Resour* 34(4):448–467
- Fatichi S, Ivanov VY, Caporali E (2013) Assessment of a stochastic downscaling methodology in generating an ensemble of hourly future climate time series. *Clim Dyn* 40(7–8):1841–1861
- Fischer EM, Knutti R (2014) Detection of spatially aggregated changes in temperature and precipitation extremes. *Geophys Res Lett* 41(2):547–554
- Fischer EM, Beyerle U, Knutti R (2013) Robust spatially aggregated projections of climate extremes. *Nat Clim Change* 3(12):1033–1038
- Fischer EM, Sedlacek J, Hawkins E, Knutti R (2014) Models agree on forced response pattern of precipitation and temperature extremes. *Geophys Res Lett* 41:8554–8562
- Frankcombe LM, England MH, Mann ME, Steinman BA (2015) Separating internal variability from the externally forced climate response. *J Clim* 28(20):8184–8202
- Giorgi F, Mearns LO (2002) Calculation of average, uncertainty range, and reliability of regional climate changes from AOGCM simulations via the “reliability ensemble averaging” (REA) method. *J Clim* 15(10):1141–1158
- Hawkins E, Sutton R (2009) The potential to narrow uncertainty in regional climate predictions. *Bull Am Meteor Soc* 90(8):1095–1108
- Hawkins E, Sutton R (2010) The potential to narrow uncertainty in projections of regional precipitation change. *Clim Dyn* 37(1–2):407–418
- Hawkins E, Smith RS, Gregory JM, Stainforth DA (2015) Irreducible uncertainty in near-term climate projections. *Clim Dyn* 46(11–12):3807–3819
- Hingray B, Said M (2014) Partitioning internal variability and model uncertainty components in a multimember multimodel ensemble of climate projections. *J Clim* 27(17):6779–6798
- Hu K, Huang G, Xie S-P (2018) Assessing the internal variability in multi-decadal trends of summer surface air temperature over East Asia with a large ensemble of GCM simulations. *Clim Dyn* 52:6229–6242
- IPCC (2013) Climate change 2013: the physical science basis. In: Contribution of working group I to the fifth assessment report of the intergovernmental panel on climate change. Cambridge University Press, Cambridge
- Ivanov VY, Bras RL, Curtis DC (2007) A weather generator for hydrological, ecological, and agricultural applications. *Water Resour Res* 43:W10406. <https://doi.org/10.1029/2006WR005364>
- Kang I-S, Shukla J (2006) Dynamic seasonal prediction and predictability of the monsoon. In: Wang B (ed) *The Asian monsoon*. Springer, Berlin, pp 585–612
- Kim J, Ivanov VY (2015) A holistic, multi-scale dynamic downscaling framework for climate impact assessments and challenges of addressing finer-scale watershed dynamics. *J Hydrol* 522:645–660
- Kim J, Ivanov VY, Fatichi S (2016a) Soil erosion assessment—Mind the gap. *Geophys Res Lett* 43(24):12446–412456
- Kim J, Ivanov VY, Fatichi S (2016b) Climate change and uncertainty assessment over a hydroclimatic transect of Michigan. *Stoch Env Res Risk A* 30(3):923–944
- Kim J, Ivanov VY, Fatichi S (2016c) Environmental stochasticity controls soil erosion variability. *Sci Rep* 6(1):22065
- Kim J, Tanveer ME, Bae DH (2018) Quantifying climate internal variability using an hourly ensemble generator over South Korea. *Stoch Env Res Risk A* 32(11):3037–3051
- Kim J, Lee J, Kim D, Kang B (2019) The role of rainfall spatial variability in estimating areal reduction factors. *J Hydrol* 568:416–426
- Lafaysse M, Hingray B, Mezghani A, Gailhard J, Terray L (2014) Internal variability and model uncertainty components in future hydrometeorological projections: the alpine durance basin. *Water Resour Res* 50(4):3317–3341
- Martel J-L, Mailhot A, Brissette F, Caya D (2018) Role of natural climate variability in the detection of anthropogenic climate change signal for mean and extreme precipitation at local and regional scales. *J Clim* 31(11):4241–4263
- Moise AF, Hudson DA (2008) Probabilistic predictions of climate change for Australia and southern Africa using the reliability ensemble average of IPCC CMIP3 model simulations. *J Geophys Res Atmos* 113:D15113. <https://doi.org/10.1029/2007JD009250>
- Monerie P-A, Sanchez-Gomez E, Pohl B, Robson J, Dong B (2017) Impact of internal variability on projections of Sahel precipitation change. *Environ Res Lett* 12(11):114003
- Olonscheck D, Notz D (2017) Consistently estimating internal climate variability from climate model simulations. *J Clim* 30(23):9555–9573
- Peleg N, Molnar P, Burlando P, Fatichi S (2019) Exploring stochastic climate uncertainty in space and time using a gridded hourly weather generator. *J Hydrol* 571:627–641

- Pendergrass AG, Knutti R, Lehner F, Deser C, Sanderson BM (2017) Precipitation variability increases in a warmer climate. *Sci Rep* 7(1):17966
- Scaife AA, Smith D (2018) A signal-to-noise paradox in climate science. *npj Clim Atmos Sci* 1(1):1–8
- Schindler A, Toreti A, Zampieri M, Scoccimarro E, Gualdi S, Fukutome S, Xoplaki E, Luterbacher J (2015) On the internal variability of simulated daily precipitation. *J Clim* 28(9):3624–3630
- Simmons AJ, Hollingsworth A (2002) Some aspects of the improvement in skill of numerical weather prediction. *Q J Roy Meteor Soc* 128(580):647–677
- Tebaldi C, Smith RL, Nychka D, Mearns LO (2005) Quantifying uncertainty in projections of regional climate change: a Bayesian approach to the analysis of multimodel ensembles. *J Clim* 18(10):1524–1540
- Thompson DWJ, Barnes EA, Deser C, Foust WE, Phillips AS (2015) Quantifying the role of internal climate variability in future climate trends. *J Clim* 28(16):6443–6456
- Tran VN, Kim J (2019) Quantification of predictive uncertainty with a metamodel: toward more efficient hydrologic simulations. *Stoch Env Res Risk A* 33(7):1453–1476
- Von Storch H, Zwiers FW (2001) *Statistical analysis in climate research*. Cambridge University Press, Cambridge
- Wang L, Deng A, Huang R (2018) Wintertime internal climate variability over Eurasia in the CESM large ensemble. *Clim Dyn* 52:6735–6748
- Wilson EB, Hilferty MM (1931) The distribution of chi-square. *Proc Natl Acad Sci U S A* 17(12):684–688
- Xie S-P et al (2015) Towards predictive understanding of regional climate change. *Nat Clim Change* 5(10):921–930
- Zhang L, Wang C (2013) Multidecadal North Atlantic sea surface temperature and Atlantic meridional overturning circulation variability in CMIP5 historical simulations. *J Geophys Res Oceans* 118(10):5772–5791

Publisher's Note Springer Nature remains neutral with regard to jurisdictional claims in published maps and institutional affiliations.